Deep-Sea Research Part I 140 (2018) 14–25

Contents lists available at ScienceDirect

Deep-Sea Research Part I

journal homepage: www.elsevier.com/locate/dsri

CCE II: Spatial and interannual variability in export efficiency and the biological pump in an eastern boundary current upwelling system with substantial lateral advection

Thomas B. Kelly[a,b,*], Ralf Goericke[c], Mati Kahru[c], Hajoon Song[d], Michael R. Stukel[a,b]

[a] Earth, Ocean & Atmospheric Studies, Florida State University, Tallahassee, FL, USA
[b] Center for Ocean-Atmospheric Prediction Studies, Florida State University, Tallahassee, FL, USA
[c] Integrative Oceanography Division, Scripps Institution of Oceanography, La Jolla, CA, USA
[d] Department of Atmospheric Sciences, Yonsei University, Seoul, South Korea

1. Introduction

The biological carbon pump (BCP), a mechanism whereby atmospheric CO_2 is fixed into organic matter by marine phytoplankton and transported into the deep ocean, is responsible for the removal of 5 – 13 Pg C yr^{-1} from the atmosphere (Henson et al., 2011; Laws et al., 2011, 2000). Future changes in the BCP could thus cause a substantial perturbation to the global carbon cycle. Unfortunately, our ability to predict such changes is hampered by the large uncertainty in the current magnitude of the BCP and by the dearth of studies that have assessed interannual variability in particle flux out of the euphotic zone. While important contributions have been made by time series studies in the oligotrophic North Pacific and Sargasso Sea (Church et al., 2013; Lomas et al., 2013), there remains a critical need for research focusing on process-oriented quantification of interannual variability in the BCP, especially in dynamic coastal regions.

The BCP consists of several distinct processes including sinking, vertical mixing and subduction of organic matter, and active transport by vertically-migrating organisms (Ducklow et al., 2001; Steinberg and Landry, 2017). For this study, only gravitationally mediated flux of particulate organic carbon (POC) is considered (hereafter termed "export"). Globally, both net primary production (NPP) and export are contingent on a variety of chemical, physical and biological processes (Ducklow et al., 2001; Turner, 2015) such as nutrient availability (Cermeño et al., 2008), heterotrophic bacterial abundance (del Giorgio and Duarte, 2002), and water column stability (Sarmiento et al., 1998). Uncertainties in the global budget thus stem from complex and region-specific relationships between net primary productivity (NPP) and export production. Satellite observations provide a unique platform from which synoptic, global time series can be calculated given the use of suitable models. However, while current export models have the ability to estimate broad spatial patterns in export, they struggle to predict intra-regional variability in export efficiency (Stukel et al., 2015). Remote sensing models for export production typically encapsulate either specific mechanisms (e.g., aggregation of microphytoplankton, mesozooplankton grazing, or mineral ballasting; Armstrong et al., 2002, Siegel et al., 2014) or generalized empirical relationships (e.g., Dunne et al., 2005; Laws et al., 2011). In comparison, models of NPP have enjoyed success in predicting regional patterns (Kahru et al., 2009; Jacox et al., 2015) thanks to both strong coupling between NPP and other ecosystem variables and to an extensive in situ dataset to which to compare the models. Improved regional models are clearly a prerequisite for reducing the uncertainty within global budgets and allowing for more accurate predictions of the marine carbon cycle under different climate change scenarios.

The California Current Ecosystem (CCE) is an eastern boundary current ecosystem with both coastal boundary and wind-stress curl upwelling, and substantial offshore advection influenced by Ekman transport. Spatial gradients in export efficiency (defined herein as the ratio of export to NPP) in the CCE (moderate in coastal regions and higher offshore; Stukel et al., 2011, 2013) do not agree with the patterns predicted by some common export models which assume negligible horizontal advection or strong local coupling between NPP and export production (e.g. Dunne et al., 2005). The combination of large horizontal gradients in POC, Chl-*a*, and biomass (Goericke and Ohman, 2015; Ohman et al., 2013) with strong surface currents requires consideration of spatiotemporal decoupling in water column processes (Olivieri and Chavez, 2000; Plattner, 2005). In fact, within the CCE-LTER dataset there is an inverse relationship between export efficiency as measured by sediment traps and ^{14}CPP (Stukel et al., 2013; Morrow et al., in this issue), a pattern inconsistent with general expectations that are incorporated into many remote-sensing models of export production.

In this paper, we first investigate mechanistic relationships between water column processes and carbon export measured during Lagrangian experiments conducted on a series of CCE LTER cruises. These cruises were planned to sample different sources of ecosystem variability including onshore-offshore productivity gradients, ENSO phases, and

* Corresponding author at: Earth, Ocean & Atmospheric Studies, Florida State University, Tallahassee, FL, USA.
E-mail address: tbk14@fsu.edu (T.B. Kelly).

https://doi.org/10.1016/j.dsr.2018.08.007
Received 16 January 2018; Received in revised form 3 August 2018; Accepted 16 August 2018
Available online 18 August 2018
0967-0637/ © 2018 Elsevier Ltd. All rights reserved.

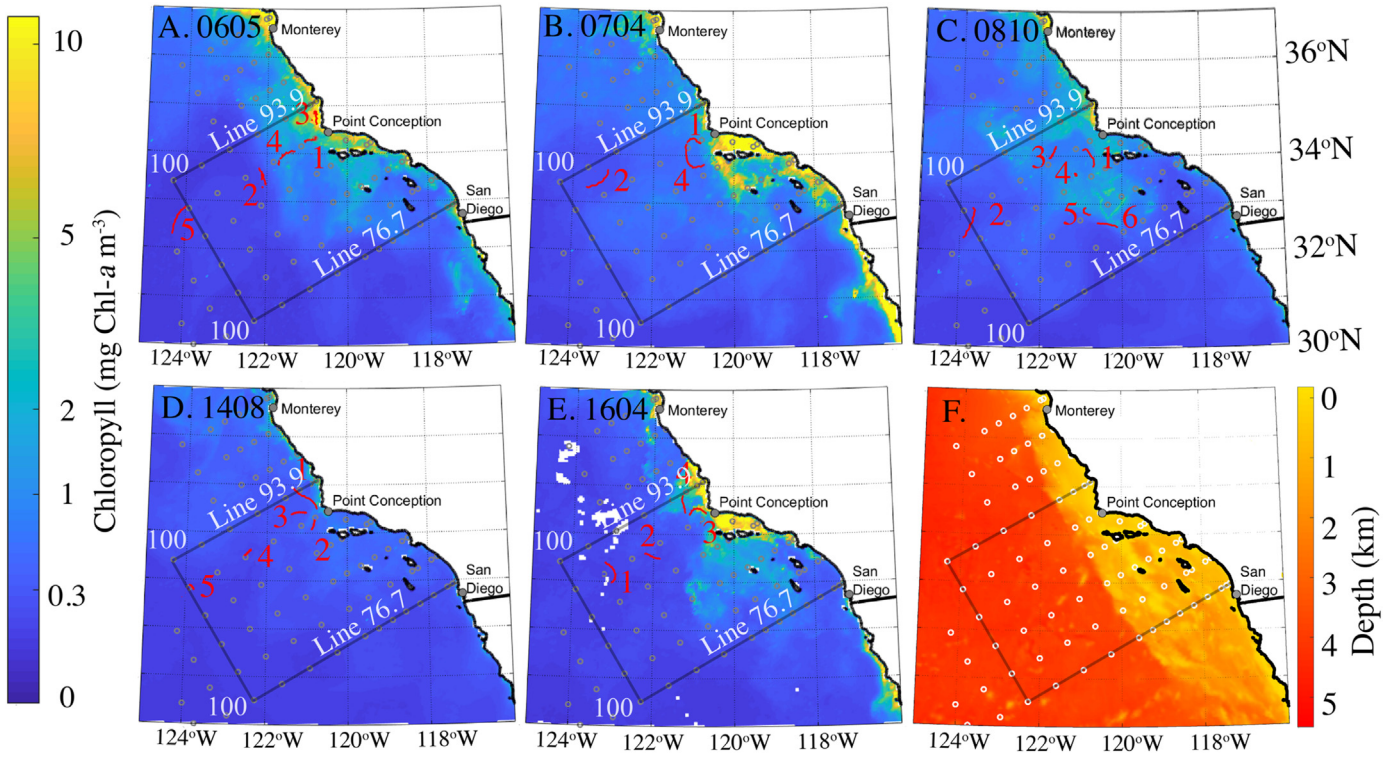

Fig. 1. CCE LTER Domain and Drifter Tracks. Each panel is a map of CCE domain (box outline) along with the CalCOFI survey grid (grey circles in A-E; white circles in F) and drifter tracks (numbered red lines) for each cycle: A. P0605, B. P0704, C. P0810, D. P1408, E. P1604. F. Bathymetric map of the study region. SSChl-*a* concentrations are shown in the shading for A-E while depth is shown in F.

seasonal climatological patterns. We then develop an empirical model to predict export and export efficiency across these different conditions. The model is then compared to several alternative formulations each representing a specific hypothesis. The model is applied to remote sensing measurements to calculate regional maps of export efficiency and export production and compared with previously published model results. Of particular importance are the regional patterns of export production and export anomalies from 1998 through 2016 (including the 2014–2015 warm anomaly and the 2015–16 El Niño).

2. Methods

2.1. Cruise data

Data used to parameterize the model came from five cruises of the California Current Ecosystem Long Term Ecological Research (CCE LTER) program: P0605 (May 2006), P0704 (April 2007), P0810 (October 2008), P1408 (August 2014), and P1604 (April 2016). Each cruise was designed to quantify ecosystem rates within homogenous water parcels representing different regions of the CCE (Fig. 1). This was accomplished through a quasi-Lagrangian drifter framework over 2–5 day periods (Landry et al., 2009, 2012) involving sediment traps, an in situ incubation array, and repeated water column surveys. In each case selection of water parcels for drifter deployment was guided by free-fall Moving Vessel Profiler surveys (Ohman et al., 2012). Key measurements used in this study include primary production ($H^{14}CO_3$-uptake; Morrow et al., in this issue) and gravitational particle export (sediment traps and ^{238}U-^{234}Th disequilibrium, Stukel et al., 2011, 2012, 2013). The present study makes use of results from 22 Lagrangian experiments, including 63 days of drifting sediment trap deployments (8 – 22 tubes per deployment), 542 ^{234}Th:^{238}U measurements and 602 primary production measurements. Bulk rates and associated errors for the 2–5 day Lagrangian experiments (hereafter 'cycles') were calculated through averaging these profiles for each experimental cycle (Table 1).

The Lagrangian framework provides contemporaneous measurements of multiple ecosystem variables over short biological timescales, thereby providing a snapshot of the ecosystem state within defined water parcels. The five cruises were designed to sample a wide range of physical and biogeochemical gradients within the CCE domain: sea surface temperature ranged from 12.2 °C to 19.8 °C, NPP ranged from 119 mg C m^{-2} d^{-1} to 4170 mg C m^{-2} d^{-1}, and sediment trap export at 100 m ranged from 32 to 299 mg C m^{-2} d^{-1} (for data source, see Section 4). The cycle locations spanned the dominant ecological gradient in the region from coastal upwelling to offshore oligotrophic (Fig. 1). While the P0605, P0704, and P0810 cruises all occurred during El Niño neutral conditions (hereafter "cool" years), the P1408 and P1604 cruises occurred during anomalously warm SST periods coinciding with an anomalous warming pattern in the northeast Pacific during 2014–2015 and the 2015–16 El Niño, respectively (Bond et al., 2015; Di Lorenzo and Mantua, 2016; Jacox et al., 2016). Within this study, the CCE domain is defined by the standard CCE control volume: the bounding box formed by CalCOFI line 76.7 out to Station 76.7–100 and line 93.9 out to Station 93.9–100 (Fig. 1). This volume is a practical boundary for spatial integrations.

2.1.1. Primary productivity

Primary productivity during each cycle was measured through in situ $H^{14}CO_3$ incubations conducted at 6–8 depths spanning the euphotic zone. Water samples were transferred from a Niskin bottle into polycarbonate incubation bottles using silicon tubing. Incubations were conducted in either 4 L polycarbonate bottles (P0605, P0704, P0810) or triplicate 250 mL bottles (P1408 and P1604). Dark bottle incubations were conducted to correct for non-photosynthetic bicarbonate utilization and/or adsorption onto particles. All samples were incubated on our Lagrangian array at the depth from which they were sampled. After approximately 24 h, incubations were retrieved and filtered onto GF/F filters, placed in liquid scintillation cocktail, and counted for ^{14}C activity. Vertically-integrated primary production was determined by

Table 1
Environmental conditions, water column parameters and sediment trap fluxes for each cruise cycle. NPP, Chl-*a*, POC are integrated over the euphotic zone. Export was calculated based on sediment trap derived flux and normalized to the base of the euphotic zone using a remineralization correction: $Export = SedTrap * \exp((Z_{SedTrap} - Z_{eu}) \bullet 0.0063)$. Export during P0605 cycles (*) was based on ^{234}Th:^{238}U disequilibrium profiles and not sediment traps. Data is available from the CCE Datazoo site (see Section 4 for data source).

Cruise/Cycle	Distance Offshore (km)	NPP (mg C m^{-2} d^{-1})	Chl (mg Chl-*a* m^{-2})	POC (mg C m^{-2})	SST (C)	SedTrap Depth (m)	SedTrap (mg C m^{-2} d^{-1})	Euphotic Depth (m)	Export (mg C m^{-2} d^{-1})
CCE-P0605–2	109	522 (9)	27 (3)	4730 (280)	14.6	–	–	78	72 (12) *
CCE-P0605–4	14	1442 (252)	50 (10)	5400 (870)	14.8	–	–	32	133 (13) *
CCE-P0605–5	63	458 (153)	31 (8)	4880 (750)	16.4	–	–	63	76 (19) *
CCE-P0704–1	26	1215 (829)	67 (21)	5300 (1550)	12.4	100	144 (6)	42	207 (9)
CCE-P0704–2	175	573 (84)	31 (7)	5120 (340)	14.2	100	32 (3)	65	40 (4)
CCE-P0704–4	50	2295 (916)	74 (13)	6730 (960)	12.4	100	170 (20)	49	234 (28)
CCE-P0810–1	41	551 (180)	55 (41)	5140 (1900)	17	50	112 (17)	41	119 (18)
CCE-P0810–2	220	478 (31)	23 (2)	4040 (530)	16.9	100	69 (6)	58	89 (8)
CCE-P0810–3	70	888 (79)	40 (3)	4500 (1390)	15.9	60	120 (6)	41	136 (7)
CCE-P0810–4	70	672 (85)	80 (21)	9250 (1550)	16	50	216 (2)	28	248 (3)
CCE-P0810–5	127	1670 (307)	66 (9)	5600 (420)	15.0	60	127 (14)	29	155 (17)
CCE-P0810–6	177	316 (41)	21 (3)	3020 (290)	17.2	60	112 (12)	58	114 (13)
CCE-P1408–1	24	386 (106)	117 (33)	9700 (2050)	16.8	60	159 (3)	30	192 (4)
CCE-P1408–2	42	320 (9)	56 (10)	7670 (1480)	16.8	60	124 (7)	35	145 (8)
CCE-P1408–3	52	280 (10)	31 (3)	5160 (350)	18.6	60	111 (7)	44	123 (7)
CCE-P1408–4	200	119 (10)	20 (2)	3520 (350)	19.1	70	51 (2)	56	56 (2)
CCE-P1408–5	355	132 (5)	18 (1)	3620 (390)	19.8	100	42 (1)	75	50 (1)
CCE-P1604–1	278	220 (55)	31 (2)	5010 (710)	17.5	100	72 (4)	73.5	85 (4)
CCE-P1604–2	174	261 (63)	27 (1)	4140 (110)	15.3	97	40 (2)	86	43 (2)
CCE-P1604–3	55	865 (228)	52 (8)	6730 (2030)	13.4	57	120 (5)	43	131 (5)
CCE-P1604–4	18	1658 (339)	116 (19)	13750 (4400)	14.4	47	251 (4)	16	305 (5)

trapezoidal integration.

2.1.2. Sediment trap

We used drifting VERTEX-style sediment traps with an 8:1 aspect ratio (height: diameter) topped by a baffle constructed from smaller tubes with a similar 8:1 aspect ratio (Knauer et al., 1979). During each experimental cycle (except on cruise P0605), cross frames consisting of 8 or 12 trap tubes were deployed at 100 m (sometimes an additional cross frame was deployed at 50–60 m depending on the maximum extent of the euphotic zone estimated at sea by CTD fluorescence). All trap deployments were deeper than the mixed layer depth. Tubes were filled with a hypersaline, poisoned brine solution (0.4% formaldehyde final concentration). Upon recovery, the overlying seawater was gently siphoned before the samples were split for analysis using a Folsom splitter: C and N were measured with a CHN analyzer or isotope ratio mass spectrometer, C:^{234}Th ratios were determined as described below, and pigments (Chl-*a* and pheopigments) were measured by the acidification method. See Stukel et al. (2013) and Morrow et al., (in this issue) for more details.

Measured export was normalized to the base of the euphotic zone by assuming exponential decrease in export flux with depth: $f_{eup} = f_{sedtrap} \bullet \exp(\gamma \Delta d)$ where γ is the remineralization length coefficient (averaging 0.0063 m^{-1} in the shallow CCE; Stukel et al., 2015) and Δd is the separation between the base of the euphotic zone (defined as the 1% light level averaged over multiple CTD casts for each cycle) and the sediment trap depth (typically either 50 m, 60 m or 100 m). This led to a maximum change of 44% in measured export (Cycle P0704-1) and an average change of 15% across entire dataset. P0605 data (based only on ^{234}Th since sediment traps were not utilized; see below) was not corrected in this manner. Instead ^{234}Th:^{238}U disequilibrium was integrated over the euphotic depth.

2.1.3. Thorium export measurements

During all cruises, ^{234}Th:^{238}U disequilibrium measurements were taken using the standard small volume method (Benitez-Nelson et al., 2001; Pike et al., 2005). Vertical ^{234}Th profiles were then used in a steady-state export model (see Savoye et al., 2006 and references therein) with C:^{234}Th ratios determined from > 50-μm particles collected by in situ pumping (McLane Industries) at 100 m for P0605 and from particles collected in the sediment trap on subsequent cruises.

2.2. Remote sensing products

Merged satellite data products for SST, Chl-*a*, NPP, and POC have been developed for the CCE-LTER domain (http://www.wimsoft.com/CC4km.htm). The Chl-*a* product is empirically optimized for this region (Kahru et al., 2012, 2015) and merged from multiple sensors (OCTS 1996–1997, SeaWiFS 1997–2010, MERIS 2002–2012, MODIS-Aqua 2002-present, and VIIRS 2012-present) with a spatial resolution of 4 km. NPP is based on the derived Chl-*a* and multi-sensor merged PAR data using a modified VGPM model (Kahru et al., 2009). Monthly composited average fields were used throughout to reduce gaps due to cloud cover. Regional maps of the diffuse attenuation coefficient ($K_{D,490}$) were retrieved from the NASA ocean color website (https://oceancolor.gsfc.nasa.gov/) with the same spatial and temporal scales.

2.3. Model framework & hydrodynamic model

The goal of this paper is to develop a model that can be used to predict interannual variability in export flux in the CCE. It is crucial that such a model be capable of capturing intra-regional variability in export. We make the assumption that functional relationships between ecosystem processes and physical drivers are consistent within the region, thus we can make a “space-for-time” assumption and utilize the broad spatial variability across the region to elucidate relationships between export under different productivity regimes. This assumption is supported by results showing that the functional relationships between export, primary productivity, and mesozooplankton grazing remained similar between El Niño neutral phases, the 2014–2015 North Pacific warming event and subsequent 2015–2016 El Niño, and across seasons (Morrow et al., in this issue). We analyzed an empirical relationship between export and various ecological drivers which led to a parameterization tuned for the CCE region. A linear functional form was used as there was no evidence that a different form would be better suited. A type II ordinary least squares (type II OLS) regression was used when applying the model for prediction while a type II major axis (type II MA) regression was used to assess the relationships within the cruise data.

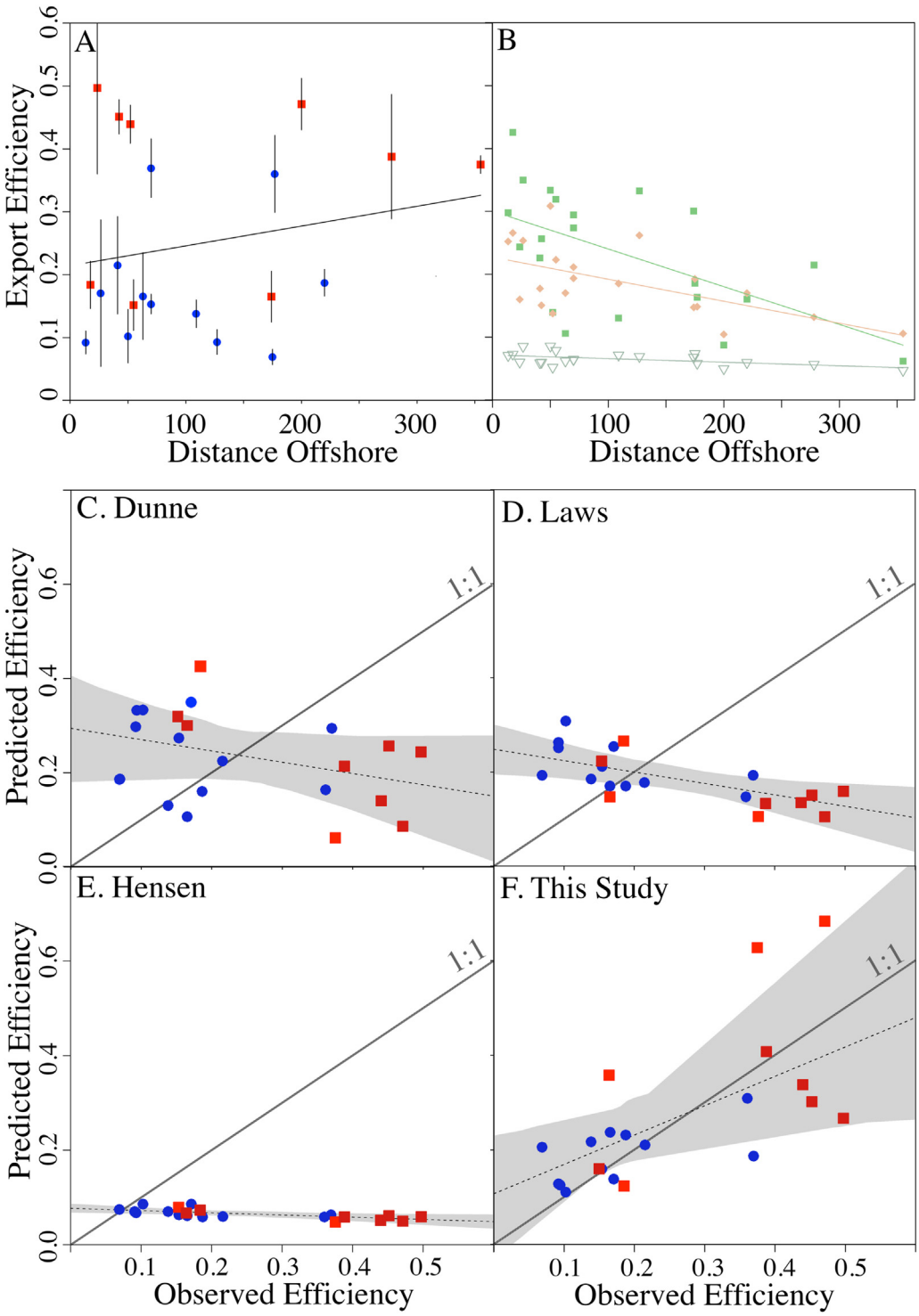

Fig. 2. A. Plot of observed e-ratios against distance offshore. "Warm" and "Cool" years are shown as red circles and blue squares respectively. Line shows least-squares linear regression. B. Same as in (A) for predicted e-ratios. Points show the Dunne et al. (green squares), Laws et al. (orange squares) and Henson et al. (green open triangles) model predictions along with least-squares linear regressions. B. Plot of predicted e-ratio from Dunne et al. export model against observed e-ratios (same legend as A). Labeled line is 1:1 correspondence. D and E. Same as (C) for the Hensen et al. and Laws et al. export models, respectively. F. Same as (C, D, E) for the model proposed in this study. Linear regressions and 95% CI are shown for each of the models (C, D, E, F; grey).

2.3.1. Sea surface temperature-advection relationship

The relationship between regional advection and SST was quantified using a 1/10th degree Regional Ocean Modeling System (ROMS) simulation, which was run for a three-month period ending with the cruise period (hereafter "3-month run"). Initial and boundary conditions for the ROMS simulation were from the CCS 31-year historical reanalysis (http://oceanmodeling.ucsc.edu/reanalccs31/) for the time period prior to 2010 and the near-real-time CCS estimation (http://oceanmodeling.ucsc.edu/ccsnrt/) for dates after 2010. Atmospheric forcing were derived from Coupled Ocean/Atmospheric Mesoscale Prediction System (COAMPS). The 3-month run model was compared to a one-month duration 4DVARS data-assimilative ROMS model which was tuned to observed cruise conditions and used the same boundary conditions as above. Since the comparison between the two simulations yielded nearly identical results, the 3-month run was used instead of the 4DVARS model for all cruises (except for P0704 where the 4DVARS model was used) in order to have sufficient run-time for analysis (see below). The ROMS simulation starts approximately 2 months before each cruise and continues until the end of the cruise.

The Larval TRANSport (LTRANS) software package is an offline, Lagrangian particle tracking model designed for integration with ROMS to allow for tracking of particle position and characteristics over time

(North et al., 2006). It was used here to track neutrally-buoyant particles within the water column. Initially particles were released at the location and time of each cycle evenly throughout the euphotic zone. The model was run backward in time, thus tracking the history of each water parcel occupied on the five cruises used in this study. The age of the water mass was defined as the median time since each particle had originally entered the euphotic zone. Euphotic depth was calculated from $K_{D,490}$ as in Tang et al. (2007) and tuned for the CCE region by comparing predicted euphotic depth (1% PAR) to in situ measurements: $z_{eu} = \frac{1.54}{K_{D,490}} + 35$.

For each cycle, 10,000 particles were released of which 58% (mean; range: 14—100%) left the euphotic zone during the simulation. Water parcel age was calculated as the median time between when the particles entered the euphotic zone and the cruise cycle occurred. For cycles where less than 50% of the particles exited the euphotic zone during the model run, age was estimated by assuming constant particle exchange between the euphotic zone and the deeper water column: $Age_{predicted} = Age_{obs}(\frac{N_{exchanged}}{N_{total}})^{-1}$ where Age_{obs} is the median age of the particles that left the euphotic zone, and $N_{exchanged}$ and N_{total} are number of particles exchanged and in total (i.e. 10,000), respectively. Comparisons between the two hydrodynamic models (3-month run and the 4DVARS run) showed that contemporaneous velocity fields were highly correlated and led to similar particle trajectories when applied to analogous LTRANS initializations.

2.4. Statistical analysis

Confidence intervals for both types of models (type II OLS and type II MA, *see* 2.3) were calculated through a non-parametric bootstrapping procedure: 10,000 distinct datasets were computed using a random, paired sampling of new (x, y) coordinates based on a normal distribution centered on the observation with a standard deviation equal to measurement uncertainty (σ_x, σ_y). The model was then fit to each dataset resulting in a distribution of the slope and intercept at each value. Model uncertainty is defined to be the 1 SE interval from the bootstrap analysis (68% confidence window for a normal distribution) averaged over the input data set. This metric provides a single number comparison between the variance in the dependent variable over the observed range of the independent variable.

3. Results and discussion

3.1. Spatial patterns in export production

Observed NPP and export production were highest in the coastal upwelling region (Table 1). However, the *e*-ratio (=export/NPP) followed an inverse relationship with elevated *e*-ratios offshore and low *e*-ratios along the coast (Fig. 2 A,B). While most hypotheses regarding ecosystem efficiency predict high *e*-ratios in productive coastal waters (e.g. Buesseler and Boyd, 2009; Michaels and Silver, 1988), the only nearshore water parcels with high *e*-ratios (> 25%) in this study were encountered during the P1408 cruise when primary productivity was depressed throughout the CCE. Indeed, primary productivity even in these nearshore cycles in August 2014 (P1408-1 & 3) exhibited values that were more representative of oligotrophic offshore regions (280–386 mg C m^{-2} d^{-1}, Table 1) than conditions typically encountered in the coastal upwelling zone. Across the dataset, we found a strong negative correlation between *e*-ratio and NPP ($P < 0.001$; Fig. 3). This confirms prior results derived from independent ^{234}Th:^{238}U disequilibrium and sediment trap methodologies (Stukel et al., 2013) and agrees with intra-regional variability found in the *e*-ratio to NPP relationship measured in the Gulf of Mexico and Southern Ocean (Maiti et al., 2016, 2013).

Most published global export models have utilized SST and NPP and/or sea surface Chl (SSChl) as inputs due to the relatively straightforward algorithms used to determine these variables by satellite. We compared our cruise observations to three prominent global export models and parameterized as in Stukel et al. (2015): Dunne et al. (2005), Laws et al. (2011), and Henson et al. (2011). Identical remote sensing fields were used throughout. While the magnitude of April-May average export flux in the CCE control volume determined by the Dunne, and by the Laws models (94, and 102 mg C m^{-2} d^{-1}, respectively) was in approximate agreement with the observed export values (mean: 131 mg C m^{-2} d^{-1}, range: 40 – 305 mg C m^{-2} d^{-1}), both modeled *e*-ratio trends departed from observations (Fig. 2 C, D, E, F). Both the Laws and Dunne models predicted that the *e*-ratio would be higher in coastal regions as a result of a positive correlation of *e*-ratio with NPP. These assumed relationships between primary production and export efficiency are directly opposite to our observed relationship of an inverse correlation between NPP and *e*-ratio in the CCE (Fig. 3). The Henson model (which computes *e*-ratio as a function of temperature) predicted a nearly constant *e*-ratio across the CCE. It is thus clear that these models do not correctly represent intra-regional variability in the *e*-ratio and particle flux. Hence, we suggest that a CCE-specific algorithm is necessary. Here, we make the assumption that spatial variability in ecosystem processes driving export flux can be used as a proxy for temporal variability in these same processes (space-for-time assumption). Independent evidence based on the relationship between sediment trap material and mesozooplankton grazing suggest that carbon export within the CCE is invariant during different climatic regimes (Morrow et al., in this issue). Therefore, a single carbon export model should be appropriate for the CCE domain across inter-annual variability.

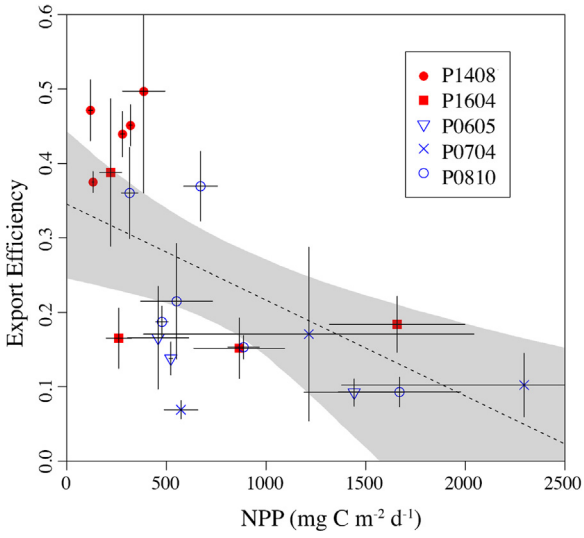

Fig. 3. Scatterplot of export efficiency against NPP for all cruise cycles. Warm cruise years and cool cruise years are shown in red and blue, respectively; while each cruise is indicated by the indicated symbol. Error bars show 1 SE of measurement uncertainty. Black dashed line is a type II MA linear fit with the 95% confidence interval shown by shading.

3.2. Observed temperature and export production

Our first step toward estimating export from satellite was to identify suitable predictors of export that can be detected using satellite remote sensing tools. Plausible predictors for export within the CCE include NPP, POC and Chl-*a* concentrations, SST, and distance offshore. All of these relationships were investigated and NPP and SST were identified as the two strongest predictors of export. A Type II OLS linear regression of *e*-ratio plotted against SST showed a significant positive slope ($P < 0.001$):

$$\text{e-ratio} = 0.056 \times SST - 0.698 \quad (1)$$

Table 2
Summary and comparison of model formulations. Statistics were calculated from a type II ordinary least squares regression. Function f is the NPP model shown, function g was applied to the residuals of f(NPP), and f′ is a function predicting e-ratio from SST (*see* 3.1.3).

Model	Formula	RMSE	R^2	Mean Conf. (95%)
SST	Export = NPP * f(SST)	62.4	0.67	29.0%
NPP	Export = m * NPP + offset	52.2	0.88	27.3%
Add 1	*Export = f(NPP) + g(SST)*	*52.2*	*0.88*	*55.4%*
Add 2	*Export = f(NPP) + g(Chl-a)*	*38.2*	*0.93*	*58.4%*
Add 3	*Export = f(NPP) + g(distance)*	*47.6*	*0.90*	*71.6%*
Add 4	*Export = f(NPP) + g(POC)*	*35.9*	*0.94*	*54.6%*

where the slope was 0.056 ± 0.008 (mean ± 1 standard error) and the intercept was − 0.698 ± 0.122. The Root Mean Squared Error (RMSE) assessing the model-data misfit was 62.4 with an R^2 of 0.67 (Table 2). Model uncertainty was 29.0% (1 SE). This positive relationship between SST and *e*-ratio was initially surprising. Increased temperature speeds up heterotrophic processes, including remineralization by heterotrophic bacteria and particle consumption by protists and metazoan zooplankton (Ikeda, 1985; Kirchman et al., 2009; Laws et al., 2000; Marsay et al., 2015). Conversely, cold temperatures in this region are indicative of upwelling and the introduction of nitrate that can support new production and eventual export (Dugdale and Goering, 1967; Eppley and Peterson, 1979). We thus find it unlikely that temperature is a direct driver of increased export efficiency. Rather, we hypothesize that temperature is a proxy for other processes affecting spatial variability in export flux in the CCE, with lateral advection as the most likely process.

Regionally, the relationship between SST and export efficiency (Fig. 4) is robust (overlapping relationships were found in both "warm" and "cool" cruise years). As a region with coastal upwelling and Ekman transport, which entrains recently upwelled water and advects it offshore, the positive correlation between SST and *e*-ratio can be explained as a mutual correlation with water mass age. As upwelling occurs, cold, nutrient-rich waters are introduced to the euphotic zone leading to high rates of NPP and biomass accumulation. The dominant advective patterns then move the water parcel offshore while nutrients are drawn down and the water gains heat from the atmosphere. As the nutrients are depleted, phytoplankton production declines but export production may remain higher than predicted (based on this reduced NPP) as a result of the time lag between particle production and particle export. When combined with offshore Ekman transport, this temporal lag drives a spatial decoupling of export and new production that has been predicted from model results (Olivieri and Chavez, 2000; Plattner, 2005) and observed in field data (Stukel et al., 2011) in the CCE.

3.2.1. *Regional advection and temperature: Advection model to explain the temperature relationship*

We suggest that the relationship between *e*-ratio and SST is not mechanistic, but instead provides a proxy for the temporal-spatial decoupling between production and export. Due to horizontal advection, coastally produced POC is rapidly transported offshore leading to depressed *e*-ratios close to shore and elevated *e*-ratios offshore. Therefore, since temporal lags drive the relationship, we can think of the controlling factor to be the age of water (defined herein as the time since the water parcel was upwelled into the euphotic zone). Upwelled water is approximately a consistent temperature and, importantly, nearly always colder than the ambient atmospheric temperature in the region, leading to positive heat flux into the water (particularly during the spring, summer and fall periods that we sampled). Due to the high heat capacity of the water, mixed-layer and euphotic zone water parcels in the CCE likely reach equilibrium temperature only after a period of weeks to months.

To assess the temperature-age relationship, we used results from a physical circulation model (ROMS) to force a particle advection model (LTRANS) that was run backward in time to determine the median length of time since each water parcel that we studied at sea entered the euphotic zone. The results of the LTRANS-ROMS simulation show the fraction of the water that was upwelled versus time for the length of the simulation (see Supp. Table 1). While the distribution of particle ages was quite variable and often multimodal (e.g. distinct events), calculating the age of the water parcel based on the median allows for a robust estimate without relying *a priori* on a particular age distribution. Comparing the LTRANS-calculated age versus SST, we find a significant ($p < 0.01$) positive relationship verifying that SST and age since upwelling covary within the CCE (Fig. 5). This supports our supposition that the SST-*e*-ratio relationship is not causal, but instead is a byproduct of the advective nature of the system. The large degree of variance within this dataset may be suggesting that either the SST *e*-ratio

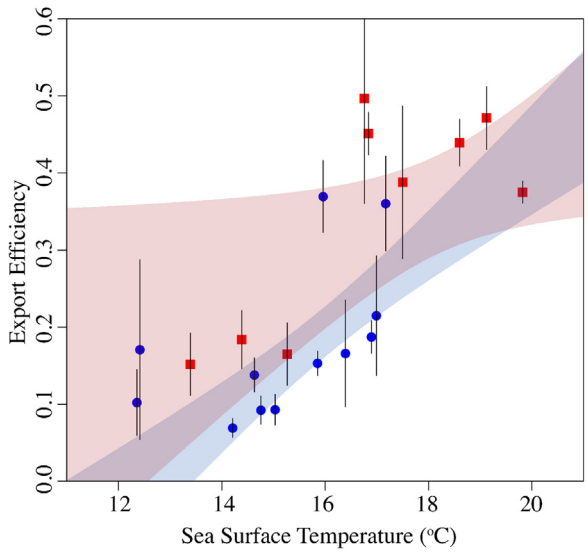

Fig. 4. Plot of *e*-ratio (Sed Trap Flux / ^{14}CPP) against SST (°C) for the indicated cruises. Colored bands indicated the 95% confidence intervals on the relationship for just the "warm" cruises (orange; P1604 and P1408) and for all cruises (blue).

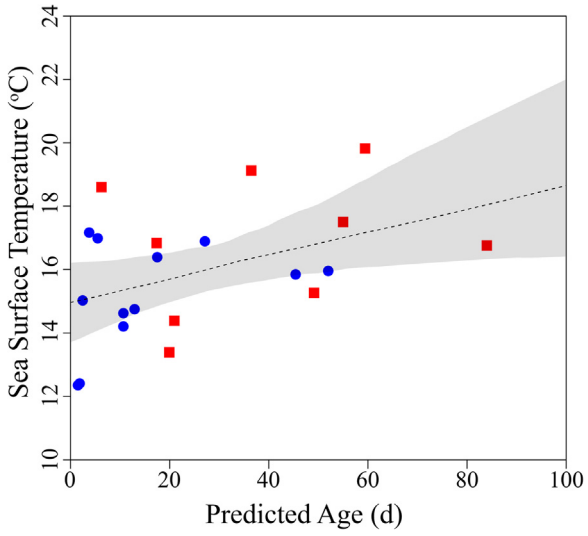

Fig. 5. Scatterplot showing age of water parcel based on LTRANS-ROMS model results against the measured SST for each cycle of P1604, P1408, P0810 and P0605 (Table 1). Dashed line is type II MA linear regression with 95% confidence interval determined from a bootstrapped jackknife procedure (sample with replacement; shaded region).

relationship is more complicated than this analysis allows for or that the LTRANS simulation fits are over-simplifying an otherwise complex time series of mixing and diffusion.

We recommend against using SST as a predictor of interannual variability in export flux in the CCE, because interannual variability in surface temperature can alter the SST-age relationship. Specifically, we should expect that during warm phases of ENSO or the Pacific Decadal Oscillation or during potentially unrelated warming events, such as the 2014 warm anomaly, surface temperatures at a given water parcel age would be warmer than if initial temperatures were cooler. An SST-based algorithm would thus inflate export estimates during periods when our mechanistic understanding of temperature-respiration relationships suggests we should expect lower export efficiency. In other words, because the SST to *e*-ratio relationship is not causal, we should not expect temporal stationarity to hold for this particular relationship.

The likelihood that the age of the water parcel and offshore advection were the ultimate drivers of the SST to *e*-ratio relationship also has important implications for our expectations of NPP to *e*-ratio relationships. If slowly sinking particles are being produced nearshore and advected offshore (or if neutrally-buoyant particles are being produced nearshore and converted into sinking particles by aggregation or compaction into mesozooplankton fecal pellets as they are advected offshore) we should expect that a portion of the NPP in coastal regions serves to support export in offshore regions.

3.3. NPP and export production

Fundamentally, NPP sets the maximum energy within an ecosystem; therefore, it is a valuable predictor of the magnitude of many ecosystem processes. Without strong evidence to support any specific functional form for the NPP-export relationship, we selected a linear fit (Eq. (2)). A type II OLS linear regression with bootstrap error suggested a statistically significant positive relationship (slope = 0.081 ± 0.021) between export and NPP with a significant ($p < 0.001$) positive intercept ($71.9 \pm 19.3\ mg\ C\ m^{-2}\ d^{-1}$).

$$Export = 0.081 \times NPP + 71.9 \quad (2)$$

This NPP-model had a Root Mean Squared Error (RMSE) of 52.2 with an R^2 of 0.88. Model uncertainty is 37.2%. The non-zero intercept can be interpreted as a background level of well-mixed POC that is produced in the coastal region and sinks slowly. Such an interpretation of the data is supported by an analysis of the sediment trap collected material. When compared to autochthonous phytoplankton production and mesozooplankton grazing, export rates remain elevated leading to positive export even as NPP tends towards zero (Fig. 6). Furthermore, this "residual" export is expected to have no pigment content, and thus is likely derived from older, recalcitrant particles (for a detailed analysis see Morrow et al., in this issue). Since the CCE region is strongly advective, slowly sinking particles may be transported considerable distances before they settle past the depth horizon sampled by the sediment traps. Across the water parcels that we sampled, the median value for the bulk turnover time of POC with respect to sinking (POC standing stock / export) was 56 days, highlighting the potential for extensive advective transport of particles prior to export. Stukel et al. (2017b) used sinking rates parameterized from in situ data and a particle transport model to estimate that in the CCE, exported POC was produced (on average) 9–78 km from where it eventually crossed the 100-m depth horizon.

While other commonly used functional relationships guarantee a zero intercept (e.g., power function), the advective nature of the CCE suggests that local export should never decrease to zero. The non-zero intercept can be interpreted as the export due to a class of slowly sinking, non-pigmented POC that becomes well-mixed within the euphotic zone due to a longer residence time compared to quicker settling particles. Importantly, this statistically robust offset highlights the decoupling between particle production and measured export of these long-lived, slowly sinking particles.

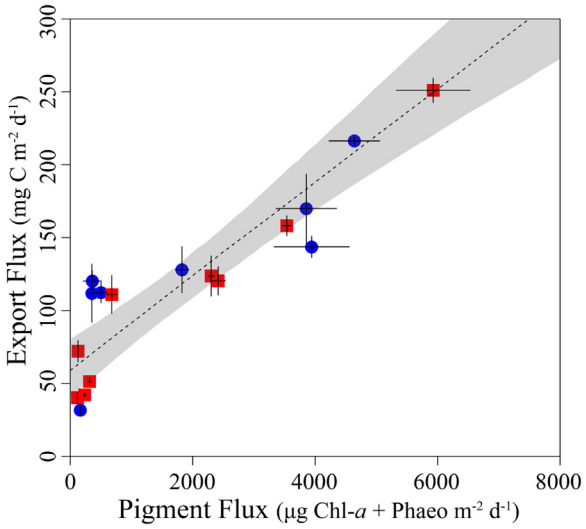

Fig. 6. Comparison of carbon export flux and bulk pigment fluxes out of the base of the euphotic zone. Pigment flux consists of the sum of Chlorophyll-*a* and phaeopigment flux estimates. Colors and symbols are as in previous figures with red squares representing anomalously warm cruise years and blue circles for anomalously cool cruise years. Error bars show 1 standard error in the measurements. Regression is type II MA regression with 95% confidence intervals shown by shading.

3.3.1. NPP-export relationship

To test the applicability of the model under different climatic conditions (i.e., to test the space-for-time assumption), we assessed the relationship's sensitivity to intra-annual (seasonal), and inter-annual (ENSO cycles) variability. The relationship proved robust across these partitionings of the dataset (Supp. Fig. 2). The 95% confidence interval on the type II linear regressions overlapped significantly in each case and a positive intercept was always found (although the intercept was not always significant at the 95% confidence interval, because fewer data points were available when the data were partitioned, Fig. 7).

Export efficiency has been found to be contingent on a number of physical drivers and ecosystem processes including water column structure, species composition, and the composition of the POC itself. The linear relationship proposed here implies that across the domain a constant proportion of primary productivity is exported as rapidly sinking particles (i.e., the slope of the regression). This is likely a generalization of a more complex relationship that varies in space and time. Hence, the empirical model (Eq. (2)) was also compared against several additional formulations involving both physical and ecosystem metrics including distance offshore, SST, and concentrations of POC and Chl-*a* (Table 2).

3.3.2. NPP model extension

While the NPP model (Eq. (2)) explains 88% of the variance in the sediment trap flux measurements (Table 2), several extensions of the model were tested using measurements with remote sensing proxies (Supp. Fig. 2). Additional variance in the flux measurements was accounted for by regressing on the residuals of the NPP model (Supp. Fig. 2). This additional explanatory power is balanced by a corresponding increase in model uncertainty. By including SST in the NPP model, model uncertainty increased from 27.3% to 55.4% without gaining any explanatory power ($R^2 = 0.88$). This lends further support to our supposition that the strong relationship between SST and *e*-ratio was in fact caused by the offshore advection of POC, which is already accounted for by our base NPP model (Eq. (2)).

The inclusion of Chl-*a* led to an increase of explanatory power (0.93) and an increase in model uncertainty (from 27.3% to 58.4%).

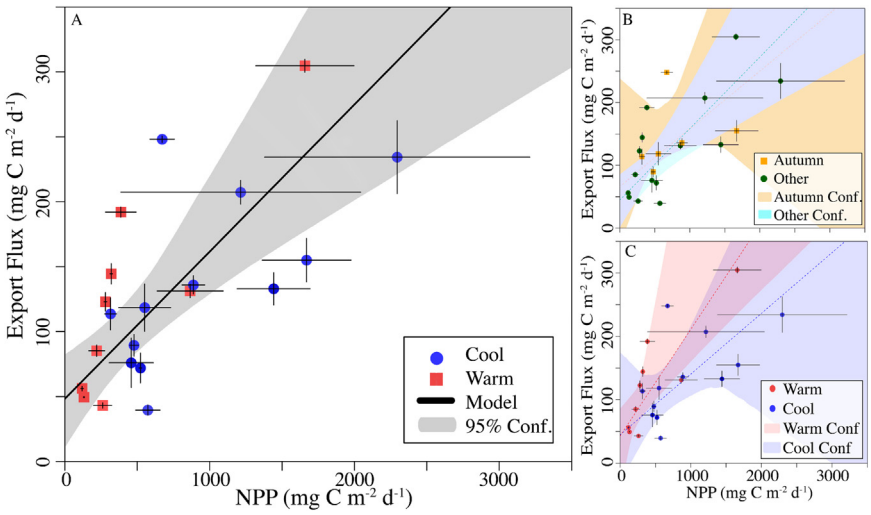

Fig. 7. A. Export flux vs Net Primary Productivity along with type II major axis regression. Error bars indicate 1 SE of measurement. Grey band is 95% confidence interval for the regression on all data. Red squares indicate data from P1604 and P1408 (i.e. "warm" years) while blue circles indicate all other cruises (P0605, P0704, and P0810; i.e. "cold" years). B. Same as in (A) showing 95% confidence windows for regression on "autumn" (P0810) cruise and the other years only (orange squares and green circles, respectively). C. Same as (A) with 95% confidence windows for warm-year and cool-year cruises (red squares and blue circles, respectively).

Similarly, adding POC led to an increased R^2 value (0.94) with an increase in uncertainty (to 54.6%). This suggests that the inclusion of these parameters is potentially useful as it reflects biomass and hence is likely related to where on the temporal sequence (i.e. new production and biomass accumulation → maximum biomass → net biomass decrease and high *e*-ratio) a particular water parcel is located. POC and Chl-*a* concentrations may thus reflect, in part, the accumulated amount of refractory biomass in the system. However, the increased uncertainty suggests that the addition of these parameters is not justified for use in a predictive model. Each additional parameter increases the risk of overfitting the model and thereby reducing its utility when extended to other parts of our regional domain. We believe a 2-parameter model is most suitable when compared to the size of the dataset (n = 22).

3.4. Interannual variability in satellite-derived export production

Fig. 8 shows April-May anomalies in export production calculated from satellite data using Eq. (2). Regional annually-averaged export production dropped from a climatological mean of 109.7 mg C m^{-2} d^{-1} to 100.3 mg C m^{-2} d^{-1} during the peak of the 2015–16 El Niño event in 2015, a decrease of 8.6%, with the largest anomalies taking place in the coastal zone (15.3% decrease; Table 3; Supp. Table 2). Similarly, in spring 1998 (during the 1997–98 El Niño), export production dropped by 7.1% regionally, with coastal zone export dropping 14.0%. These decreases in particle export were accompanied by concomitant decreases in NPP that were ultimately caused by reduced coastal upwelling (Kahru et al., 2018). While the decreased export was seen throughout the region during the 1998 El Niño, the region north of Point Conception actually experienced above-average modeled springtime NPP and export during the 2014–2015 warm anomaly and 2015–2016 El Niños. (Fig. 8). Whether this increase reflected different upwelling patterns driven by substantial differences in the physical processes associated with each El Niño (Jacox et al., 2016) is beyond the scope of this manuscript.

A full time-series of reconstructed export production in the CCE from 1998 to 2017 (Fig. 9) shows a substantial decline in export in all seasons during the 2014–2015 warm anomalies and the 2015–2016 El Niño relative to the preceding decade, particularly in the productive coastal upwelling region that drives much of the variability in export flux in the CCE. Such a result is not surprising, given the increased stratification, decreased nutrient concentrations, and decreased phytoplankton biomass observed region-wide (McClatchie et al., 2016).

3.5. Caveats, future research, and other mechanisms of export

The model embedded within Eq. (2) reflects a hypothesis about the processes driving particle flux in the CCE. Specifically, it suggests that there are two classes of sinking particles; a slowly-sinking recalcitrant particle class that reflects allochthonous particle production and is impacted by substantial horizontal advection, and a rapidly-sinking particle class that is reflective of autochthonous particle production in the water immediately above the sediment trap. Results of other studies (Stukel et al., 2013; Morrow et al., in this issue) suggest that the latter particle class is primarily composed of sinking mesozooplankton fecal pellets, while the former is likely marine snow comprised of degraded POM of unknown origin. The robustness of this relationship with regards to seasonal or interannual variability in the CCE gives us some confidence in its applicability to estimate interannual variability in export flux. However, it is important to consider that the underlying hypothesis (i.e., export driven by a combination of longer-lived particles and autochthonous production) could be represented by other functional forms. For instance, perhaps the export of longer-lived particles (which are likely derived disproportionately from the high productivity regions near the coast) is not constant, but decreases slightly with distance from shore. Indeed, when considered on longer spatial scales, such a scenario is almost certainly true - otherwise we would expect much higher export ratios in the oligotrophic subtropical gyre than are actually measured (Church et al., 2013; Neuer et al., 2002). Furthermore, it is possible that the production of rapidly-sinking particles is not a constant fraction of NPP, but instead shows a quadratic or power law relationship to NPP. Such a relationship might be expected given trophic shifts from protozoan grazers to mesozooplankton grazers when primary productivity is principally attributable to large phytoplankton. The ability to resolve a more complex model, however, will require substantially more simultaneous export and NPP measurements across the CCE.

Despite the above discussion, there are conceptual reasons to be confident that the true underlying relationship may not deviate too far from Eq. (2). First, while it might be assumed that increased Ekman transport during upwelling-favorable conditions would lead to increased particle transport offshore and hence a higher export of long-lived particles offshore, increased Ekman transport is typically accompanied by increased subduction. Thus, water parcels may spend less time at the surface and the decreased age of the water parcels may offset increased advective transport. It is thus likely that the increased Ekman transport does not drive a substantial increase in the gravitational sinking flux of recalcitrant particles, but instead leads to increased rates of POC subduction (Levy et al., 2013; Stukel et al., 2017b). Second, although it is commonly assumed that the production of labile particles should increase faster than primary production (e.g. Laws, 2004; Michaels and Silver, 1988; Siegel et al., 2014), these models often assume steady state. In a temporally dynamic, spatially

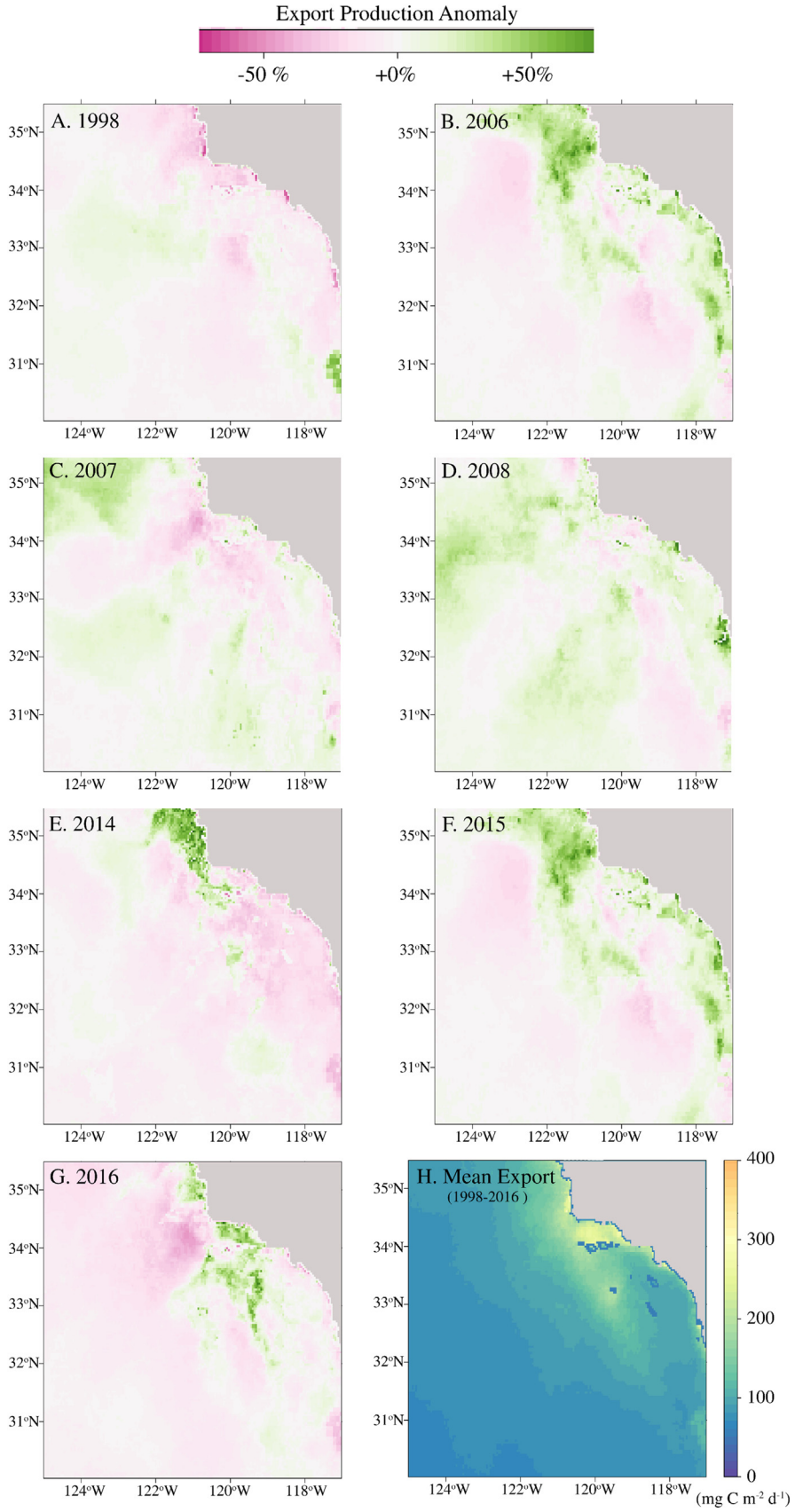

Fig. 8. Spatial map of export production anomaly (%) for April & May of the indicated year across the CCE domain based on the NPP model. Climatological values were calculated from averaging export between 1998 and 2016. (A) 1998, (B) 2006, (C) 2007, (D) 2008, (E) 2014, (F) 2015, (G) 2016. H. Spatial map of climatological April-May carbon export production (1998–2016 mean; mg C m^{-2} d^{-1}).

Table 3
Summary of CCE regional model results for select years. Shown are the modeled export production (mg C m^{-2} d^{-1}) for the region (entire CCE Domain), the coastal zone (< 150 km offshore) and the Offshore zone (> 250 km offshore) and averaged for the indicated year. Export efficiency is shown in the parentheses.

Year	Regional	Coastal Zone	Offshore
1998	101.9 (27%)	127.6 (19%)	93.2 (35%)
1999	107.3 (25%)	130.5 (18%)	99.0 (30%)
2006	111.7 (23%)	160.6 (15%)	98.1 (30%)
2007	114.2 (22%)	146.9 (16%)	105.8 (25%)
2008	115.4 (21%)	151.4 (15%)	105.7 (25%)
2014	106.0 (25%)	133.7 (15%)	97.2 (36%)
2015	100.28 (29%)	125.6 (19%)	95.4 (33%)
2016	108.2 (24%)	152.7 (15%)	98.9 (30%)

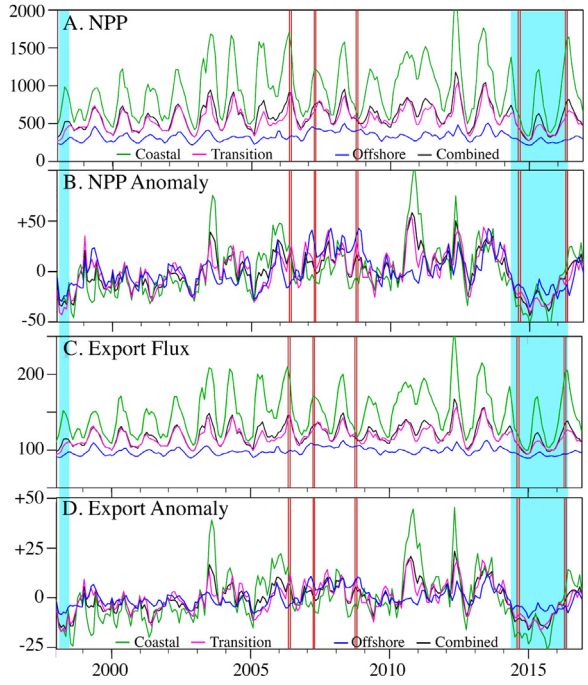

Fig. 9. (A) Time series of NPP (mg C m^{-2} d^{-1}) within the CCE domain (black), the coastal CCE waters (green), the transitional CCE waters (magenta) and the offshore CCE waters (blue). (B) Same as *A* with NPP normalized (% anomaly) to the climatological mean from 1998 to 2016. (C) Same as *A* with export flux as calculated from the model (Eq. (2)). (D) Same as *C* with export normalized (% anomaly) to the 1997–2016 climatological mean. Vertical red lines indicate each CCE-LTER cruise, while blue shaded regions are the 1997–98 and 2015–16 El Niños.

heterogeneous ocean with substantial horizontal advection, non-steady state impacts can substantially modify the NPP-export relationship. Most importantly, while we find a shift from grazing by mesozooplankton in upwelling regions to grazing by protists in oligotrophic areas, this is often accompanied by a shift in the growth: grazing balance. In coastal regions, with abundant nutrients and large diatoms, growth often exceeds grazing and the community has net biomass accumulation. In offshore regions, grazing typically exceeds growth as phytoplankton biomass declines and hence total grazing is higher than would be expected from NPP measurements. A simple trophic model used to estimate fecal pellet production from in situ measurements in the CCE actually estimated a higher ratio of fecal pellet production: NPP in the offshore region where protists dominated because of this growth: grazing imbalance (Stukel et al., 2011). It is thus possible that spatial variability in growth: grazing ratios offset spatial variability in protist: mesozooplankton grazing.

Another surprising result of our analyses relates to the balance between new and export production in warm versus neutral ENSO phases. Increased upwelling during cold years introduces additional nitrate into surface waters, leading to increased primary production and an increased *f*-ratio (new production / total production). Thus, if new production is balanced by sinking particle flux as postulated by Eppley and Peterson (1979), we would anticipate increased *e*-ratios during cold years, which is the opposite of the prediction derived from Eq. (2) and supported by our in situ measurements. However, new production and net community production (the balance of photosynthesis and ecosystem respiration, which is functionally similar to new production) are substantially higher in the CCE than export flux (Harrison et al., 1987; Stukel et al., 2013, 2011). While increased upwelling during cool ENSO phases should drive increased *f*-ratios in the region, these increased *f*-ratios are likely balanced not by increased export of sinking particles, but by an increase in other export processes (e.g., subduction and active transport; Song et al., 2012). Stukel et al. (2017a) found that subduction of suspended or slowly sinking particles was a substantial export term in the CCE, and that the aforementioned decreases in Ekman transport during warm years likely leads to decreased subduction throughout the region. Furthermore, mesoscale features (fronts and eddies) have been linked to substantial increases in subduction rates in the CCE (Stukel et al., 2017a) and the frequency of sea-surface fronts was substantially lower during the 2014–2016 marine heat wave (Kahru et al., 2018). Active transport in the CCE is primarily driven by vertically migrating euphausiids and copepods (Stukel et al., 2013). These crustaceans generally have lower biomass during warm ENSO phases and the 2014–2016 marine heat wave (Lavaniegos and Ohman, 2007; Lilly and Ohman, in this issue), suggesting decreased active transport during warm ENSO phases. Taken together, these results suggest that during El Niños, new production decreases substantially, as does active transport and passive flux of particles by subduction, while export of sinking particles shows a more moderate decline.

Our results highlight the importance of intensive, process-oriented studies and the development of region-specific algorithms for determining interannual variability in export flux. However, they also make it clear that much work remains. What is the origin, sinking speed, and remineralization rate of long-lived POM? Does mesozooplankton grazing control the production of rapidly sinking particles, or are particle formation rates and sinking speeds modulated by other processes (e.g., Fe-limitation, Brzezinski et al., 2015)? Do these results (derived from homogeneous water parcels) apply to dynamic frontal regions where export seems to be enhanced in the CCE (Krause et al., 2015; Stukel et al., 2017a)? Does recalcitrant POM flux explain inverse relationships between NPP and *e*-ratio measured in other regions (Maiti et al., 2016, 2013)? Are our results applicable to other upwelling systems, such as the Equatorial Pacific? Future progress will require spatially-resolved time-series of export flux, novel biogeochemical (Bishop et al., 2016; McDonnell et al., 2015) and ecological (Amacher et al., 2013) sampling approaches capable of assessing the mechanisms driving export flux, and new synthetic modeling approaches capable of combining such diverse observational data into predictive models of carbon flux (Coles et al., 2017; Jackson and Burd, 2015).

Acknowledgments

The work presented here was only possible with the contributions of many colleagues including seagoing personnel who make field sampling possible and data scientists who work to bring data products to the oceanographic community. We would like to thank the captain and crews of the R/V Melville, R/V Knorr, R/V Thompson and R/V Sikuliaq for their invaluable expertise and support. Thoughtful and helpful comments by two anonymous reviewers helped strengthen this manuscript. This work was funded by three NSF Bio Oce grants to the CCE LTER program: OCE-0417616, OCE-1637632 and OCE-1614359. Export and primary productivity data used in this manuscript can be

found on the CCE LTER Datazoo website: http://oceaninformatics.ucsd.edu/datazoo/catalogs/ccelter/datasets.

Appendix A. Supplementary material

Supplementary data associated with this article can be found in the online version at doi:10.1016/j.dsr.2018.08.007.

References

Amacher, J., Neuer, S., Lomas, M., 2013. DNA-based molecular fingerprinting of eukaryotic protists and cyanobacteria contributing to sinking particle flux at the Bermuda Atlantic time-series study. Deep. Res. Part II Top. Stud. Oceanogr. 93, 71–83. https://doi.org/10.1016/j.dsr2.2013.01.001.

Armstrong, R.A., Lee, C., Hedges, J.I., Honjo, S., Wakeham, S.G., 2002. A new, mechanistic model for organic carbon fluxes in the ocean based on the quantitative association of POC with ballast minerals. Deep. Res. Part II Top. Stud. Oceanogr. 49, 219–236. https://doi.org/10.1016/S0967-0645(01)00101-1.

Benitez-Nelson, C.R., Buesseler, K.O., van der Loeff, M.R., Andrews, J., Ball, L., Crossin, G., Charette, M.A., 2001. Testing a new small-volume technique for determining Th-234 in seawater. J. Radioanal. Nucl. Chem. 248, 795–799. https://doi.org/10.1023/A:1010621618652.

Bishop, J.K.B., Fong, M.B., Wood, T.J., 2016. Robotic observations of high wintertime carbon export in California coastal waters. Biogeosciences 13, 3109–3129. https://doi.org/10.5194/bg-13-3109-2016.

Bond, N.A., Cronin, M.F., Freeland, H., Mantua, N., 2015. Causes and impacts of the 2014 warm anomaly in the NE Pacific. Geophys. Res. Lett. 42, 3414–3420. https://doi.org/10.1002/2015GL063306.

Brzezinski, M.A., Krause, J.W., Bundy, R.M., Barbeau, K.A., Franks, P., Goericke, R., Landry, M.R., Stukel, M.R., 2015. Enhanced silica ballasting from iron stress sustains carbon export in a frontal zone within the California Current. J. Geophys. Res. C Ocean. 120, 4654–4669. https://doi.org/10.1002/2015JC010829.

Buesseler, K.O., Boyd, P.W., 2009. Shedding light on processes that control particle export and flux attenuation in the twilight zone of the open ocean. Limnol. Oceanogr. 54, 1210–1232. https://doi.org/10.4319/lo.2009.54.4.1210.

Cermeño, P., Dutkiewicz, S., Harris, R.P., Follows, M., Schofield, O., Falkowski, P.G., 2008. The role of nutricline depth in regulating the ocean carbon cycle. Proc. Natl. Acad. Sci. USA 105, 20344–20349. https://doi.org/10.1073/pnas.0811302106.

Church, M.J., Lomas, M.W., Muller-Karger, F., 2013. Sea change: charting the course for biogeochemical ocean time-series research in a new millennium. Deep. Res. Part II Top. Stud. Oceanogr. 93, 2–15. https://doi.org/10.1016/j.dsr2.2013.01.035.

Coles, V.J., Stukel, M.R., Brooks, M.T., Burd, A., Crump, B.C., Moran, M.A., Paul, J.H., Satinsky, B.M., Yager, P.L., Zielinski, B.L., Hood, R.R., 2017. Ocean biogeochemistry modeled with emergent trait-based genomics. Science 358 (80-.), 1149–1154. https://doi.org/10.1126/science.aan5712.

del Giorgio, P.A., Duarte, C.M., 2002. Respiration in the open ocean. Nature 420, 379–384. https://doi.org/10.1038/nature01165.

Di Lorenzo, E., Mantua, N., 2016. Multi-year persistence of the 2014/15 North Pacific marine heatwave. Nat. Clim. Chang. 6, 1042–1047. https://doi.org/10.1038/nclimate3082.

Ducklow, H.H.W., Steinberg, D.D.K., Buessler, K., Buesseler, K.O., 2001. Upper ocean carbon export and the biological pump. Oceanography 14, 50–58. https://doi.org/10.5670/oceanog.2001.06.

Dugdale, R.C., Goering, J.J., 1967. Uptake of new and regenerated forms of nitrogen in primary productivity. Limnol. Oceanogr. 12, 196–206. https://doi.org/10.4319/lo.1967.12.2.0196.

Dunne, J.P., Armstrong, R.A., Gnnadesikan, A., Sarmiento, J.L., 2005. Empirical and mechanistic models for the particle export ratio. Glob. Biogeochem. Cycles 19, 1–16. https://doi.org/10.1029/2004GB002390.

Eppley, R.W., Peterson, B.J., 1979. Particulate organic matter flux and planktonic new production in the deep ocean. Nature 282, 677–680. https://doi.org/10.1038/282677a0.

Goericke, R., Ohman, M.D., 2015. Introduction to CCE-LTER: responses of the California Current Ecosystem to climate forcing. Deep Sea Res. Part II Top. Stud. Oceanogr. 112, 1–5. https://doi.org/10.1016/j.dsr2.2014.12.001.

Harrison, W.G., Platt, T., Lewis, M.R., 1987. F-ratio and its relationship to ambient nitrate concentration in coastal waters. J. Plankton Res. 9, 235–248. https://doi.org/10.1093/plankt/9.1.235.

Henson, S.A., Sanders, R., Madsen, E., Morris, P.J., Le Moigne, F., Quartly, G.D., 2011. A reduced estimate of the strength of the ocean's biological carbon pump. Geophys. Res. Lett. 38, 10–14. https://doi.org/10.1029/2011GL046735.

Ikeda, T., 1985. Metabolic rates of epipelagic marine zooplankton as a function of body mass and temperature. Mar. Biol. 85, 543–552. https://doi.org/10.1007/BF00396409.

Jackson, G.A., Burd, A.B., 2015. Simulating aggregate dynamics in ocean biogeochemical models. Prog. Oceanogr. 133, 55–65. https://doi.org/10.1016/j.pocean.2014.08.014.

Jacox, M.G., Fiechter, J., Moore, A.M., Edwards, C.A., 2015. ENSO and the California current coastal upwelling response. J. Geophys. Res. Ocean. 120, 1691–1702. https://doi.org/10.1002/2014JC010650.

Jacox, M.G., Hazen, E.L., Zaba, K.D., Rudnick, D.L., Edwards, C.A., Moore, A.M., Bograd, S.J., 2016. Impacts of the 2015–2016 El Niño on the California Current System: early assessment and comparison to past events. Geophys. Res. Lett. 43, 7072–7080. https://doi.org/10.1002/2016GL069716.

Kahru, M., Jacox, M.G., Ohman, M.D., 2018. CCE1: decrease in the frequency of oceanic fronts and surface chlorophyll concentration in the California Current System during the 2014–2016 northeast Pacific warm anomalies. Deep Sea Res. Part I Oceanogr. Res. Pap. https://doi.org/10.1016/j.dsr.2018.04.007.

Kahru, M., Kudela, R., Manzano-Sarabia, M., Mitchell, B.G., 2009. Trends in primary production in the California Current detected with satellite data. J. Geophys. Res. Ocean. 114, 1–7. https://doi.org/10.1029/2008JC004979.

Kahru, M., Kudela, R.M., Anderson, C.R., Mitchell, B.G., 2015. Optimized merger of ocean chlorophyll algorithms of MODIS-Aqua and VIIRS. IEEE Geosci. Remote Sens. Lett. 12, 2282–2285. https://doi.org/10.1109/LGRS.2015.2470250.

Kahru, M., Kudela, R.M., Manzano-Sarabia, M., Greg Mitchell, B., 2012. Trends in the surface chlorophyll of the California. Curr.: Merging data Mult. Ocean Color Satell. Deep. Res. Part II Top. Stud. Oceanogr. 77–80, 89–98. https://doi.org/10.1016/j.dsr2.2012.04.007.

Kirchman, D.L., Morán, X.A.G., Ducklow, H., 2009. Microbial growth in the polar oceans - role of temperature and potential impact of climate change. Nat. Rev. Microbiol. 7, 451–459. https://doi.org/10.1038/nrmicro2115.

Knauer, G.A., Martin, J.H., Bruland, K.W., 1979. Fluxes of particulate carbon, nitrogen, and phosphorus in the upper water column of the northeast Pacific. Deep Sea Res. Part A, Oceanogr. Res. Pap. 26, 97–108. https://doi.org/10.1016/0198-0149(79)90089-X.

Krause, J.W., Brzezinski, M.A., Goericke, R., Landry, M.R., Ohman, M.D., Stukel, M.R., Taylor, A.G., 2015. Variability in diatom contributions to biomass, organic matter production and export across a frontal gradient in the California Current Ecosystem. J. Geophys. Res. Ocean. 120, 1032–1047. https://doi.org/10.1002/2014JC010472.

Landry, M.R., Ohman, M.D., Goericke, R., Stukel, M.R., Barbeau, K.A., Bundy, R., Kahru, M., 2012. Pelagic community responses to a deep-water front in the California Current Ecosystem: overview of the A-Front Study. J. Plankton Res. 34, 739–748. https://doi.org/10.1093/plankt/fbs025.

Landry, M.R., Ohman, M.D., Goericke, R., Stukel, M.R., Tsyrklevich, K., 2009. Lagrangian studies of phytoplankton growth and grazing relationships in a coastal upwelling ecosystem off Southern California. Prog. Oceanogr. 83, 208–216. https://doi.org/10.1016/j.pocean.2009.07.026.

Lavaniegos, B.E., Ohman, M.D., 2007. Coherence of long-term variations of zooplankton in two sectors of the California Current System. Prog. Oceanogr. 75, 42–69. https://doi.org/10.1016/j.pocean.2007.07.002.

Laws, E., 2004. Export flux and stability as regulators of community composition in pelagic marine biological communities: implications for regime shifts. Prog. Oceanogr. 60, 343–354. https://doi.org/10.1016/j.pocean.2004.02.015.

Laws, E.A., D'Sa, E., Naik, P., 2011. Simple equations to estimate ratios of new or export production to total production from satellite-derived estimates of sea surface temperature and primary production. Limnol. Oceanogr. Methods 9, 593–601. https://doi.org/10.4319/lom.2011.9.593.

Laws, E.A., Ducklow, H., McCarthy, J.J., 2000. Temperature effects on export production in the open ocean. Glob. Biogeochem. Cycles 14, 1231–1246. https://doi.org/10.1029/1999GB001229.

Levy, M., Bopp, L., Karleskind, P., Resplandy, L., Ethe, C., Pinsard, F., 2013. Physical pathways for carbon transfers between the surface mixed layer and the ocean interior. Glob. Biogeochem. Cycles 27, 1001–1012. https://doi.org/10.1002/gbc.20092.

Lilly, L.E., Ohman, M.D., CCE IV: El Niño-related zooplankton variability in the southern California Current System. Deep Sea Res. Part I Oceanogr. Res. Pap., 2018, https://doi.org/10.1016/j.dsr.2018.07.015.

Lomas, M.W., Bates, N.R., Johnson, R.J., Knap, A.H., Steinberg, D.K., Carlson, C.A., 2013. Two decades and counting: 24-years of sustained open ocean biogeochemical measurements in the Sargasso Sea. deep. Res. Part II top. Stud. Oceanogr 93, 16–32. https://doi.org/10.1016/j.dsr2.2013.01.008.

Maiti, K., Bosu, S., D'Sa, E.J., Adhikari, P.L., Sutor, M., Longnecker, K., 2016. Export fluxes in northern Gulf of Mexico - Comparative evaluation of direct, indirect and satellite-based estimates. Mar. Chem. 184, 60–77. https://doi.org/10.1016/j.marchem.2016.06.001.

Maiti, K., Charette, M.A., Buesseler, K.O., Kahru, M., 2013. An inverse relationship between production and export efficiency in the Southern Ocean. Geophys. Res. Lett. 40, 1557–1561. https://doi.org/10.1002/grl.50219.

Marsay, C.M., Sanders, R.J., Henson, S.A., Pabortsava, K., Achterberg, E.P., Lampitt, R.S., 2015. Attenuation of sinking particulate organic carbon flux through the mesopelagic ocean. Proc. Natl. Acad. Sci. 112, 1089–1094. https://doi.org/10.1073/pnas.1415311112.

McClatchie, S., Goericke, R., Leising, A.W., Auth, T.D., Bjorkstedt, E., Robertson, R., Brodeur, R.D., Du, X., Daly, E.A., 2016. State of the California Current 2015 – 16: Comparisons With the 1997 – 98 El Niño. Calif. Coop. Ocean. Fish. Investig. Rep. 57, 5–61.

McDonnell, A.M.P., Lam, P.J., Lamborg, C.H., Buesseler, K.O., Sanders, R., Riley, J.S., Marsay, C., Smith, H.E.K., Sargent, E.C., Lampitt, R.S., Bishop, J.K.B., 2015. The oceanographic toolbox for the collection of sinking and suspended marine particles. Prog. Oceanogr. 133, 17–31. https://doi.org/10.1016/j.pocean.2015.01.007.

Michaels, A.F., Silver, M.W., 1988. Primary production, sinking fluxes and the microbial food web. Deep. Res. 35, 473–490.

Morrow, R., Goericke, R., Kelly, T.B., Landry, M.R., Ohman, M.D., Stephens, B.M., Stukel, M.R., Primary Productivity, Mesozooplankton Grazing, and the Biological Pump in the California Current Ecosystem: Variability and Response to El Niño. Deep. Res. I., 2018, https://doi.org/10.1016/j.dsr.2018.07.012.

Neuer, S., Davenport, R., Freudenthal, T., Wefer, G., Llinás, O., Rueda, M.-J., Steinberg, D.K., Karl, D.M., 2002. Differences in the biological carbon pump at three subtropical ocean sites. Geophys. Res. Lett. 29, 32-1–32–4. https://doi.org/10.1029/

2002GL015393.
North, E.W., Hood, R.R., Chao, S.Y., Sanford, L.P., 2006. Using a random displacement model to simulate turbulent particle motion in a baroclinic frontal zone: a new implementation scheme and model performance tests. J. Mar. Syst. 60, 365–380. https://doi.org/10.1016/j.jmarsys.2005.08.003.
Ohman, M.D., Barbeau, K., Franks, P.J.S., Landry, M.R., Miller, A.J., 2013. Ecological Transitions in a Coastal Upwelling Ecosystem. Oceanography 26, 162–173. https://doi.org/10.5670/oceanog.2011.65.
Ohman, M.D., Powell, J.R., Picheral, M., Jensen, D.W., 2012. Mesozooplankton and particulate matter responses to a deep-water frontal system in the southern California Current System. J. Plankton Res. 34, 815–827. https://doi.org/10.1093/plankt/fbs028.
Olivieri, R.A., Chavez, F.P., 2000. A model of plankton dynamics for the coastal upwelling system of Monterey Bay, California. Deep. Res. II 47, 1077–1106. https://doi.org/10.1016/S0967-0645(99)00137-X.
Pike, S.M., Buesseler, K.O., Andrews, J., Savoye, N., 2005. Quantification of 234Th recovery in small volume sea water samples by inductively coupled plasma-mass spectrometry. J. Radioanal. Nucl. Chem. 263, 355–360. https://doi.org/10.1007/s10967-005-0062-9.
Plattner, G.-K., 2005. Decoupling marine export production from new production. Geophys. Res. Lett. 32, L11612. https://doi.org/10.1029/2005GL022660.
Sarmiento, J.L., Hughes, T.M.C., Stouffer, R.J., Manabe, S., 1998. Simulated response of the ocean carbon cycle to anthropogenic climate warming. Nature 393, 245–249. https://doi.org/10.1038/30455.
Savoye, N., Benitez-Nelson, C., Burd, A.B., Cochran, J.K., Charette, M., Buesseler, K.O., Jackson, G.A., Roy-Barman, M., Schmidt, S., Elskens, M., 2006. 234Th sorption and export models in the water column: a review. Mar. Chem. 100, 234–249. https://doi.org/10.1016/j.marchem.2005.10.014.
Siegel, D.A., Buesseler, K.O., Doney, S.C., Sailley, S.F., Behrenfeld, M.J., Boyd, P.W., 2014. Global assessment of ocean carbon export by combining satellite observations and food-web models. Glob. Biogeochem. Cycles 28, 181–196. https://doi.org/10.1002/2013GB004743.Received.
Song, H., Miller, A.J., McClatchie, S., Weber, E.D., Nieto, K.M., Checkley, D.M., 2012. Application of a data-assimilation model to variability of Pacific sardine spawning and survivor habitats with ENSO in the California Current System. J. Geophys. Res. Ocean. 117. https://doi.org/10.1029/2011JC007302.
Steinberg, D.K., Landry, M.R., 2017. Zooplankton Ocean Carbon Cycle Ann. Rev. Mar. Sci. 9, 413–444. https://doi.org/10.1146/annurev-marine-010814-015924.
Stukel, M.R., Aluwihare, L.I., Barbeau, K.A., Chekalyuk, A.M., Goericke, R., Miller, A.J., Ohman, M.D., Ruacho, A., Song, H., Stephens, B.M., Landry, M.R., 2017a. Mesoscale ocean fronts enhance carbon export due to gravitational sinking and subduction. Proc. Natl. Acad. Sci. 114, 1252–1257. https://doi.org/10.1073/pnas.1609435114.
Stukel, M.R., Kahru, M., Benitez-Nelson, C.R., Décima, M., Goericke, R., Landry, M.R., Ohman, M.D., 2015. Using Lagrangian-based process studies to test satellite algorithms of vertical carbon flux in the eastern North Pacific Ocean. J. Geophys. Res. Ocean. 120, 7208–7222. https://doi.org/10.1002/2015JC011264.
Stukel, M.R., Landry, M.R., Benitez-nelson, C.R., Goericke, R., 2011. Trophic cycling and carbon export relationships in the California Current Ecosystem. Limnol. Oceanogr. 56, 1866–1878. https://doi.org/10.4319/lo.2011.56.5.1866.
Stukel, M.R., Landry, M.R., Ohman, M.D., Goericke, R., Samo, T., Benitez-Nelson, C.R., 2012. Do inverse ecosystem models accurately reconstruct plankton trophic flows? Comparing two solution methods using field data from the California. Curr. J. Mar. Syst. 91, 20–33. https://doi.org/10.1016/j.jmarsys.2011.09.004.
Stukel, M.R., Ohman, M.D., Benitez-Nelson, C.R., Landry, M.R., 2013. Contributions of mesozooplankton to vertical carbon export in a coastal upwelling system. Mar. Ecol. Prog. Ser. 491, 47–65. https://doi.org/10.3354/meps10453.
Stukel, M.R., Song, H., Goericke, R., Miller, A.J., 2017b. The role of subduction and gravitational sinking in particle export, carbon sequestration, and the remineralization length scale in the California Current ecosystem. Limnol. Oceanogr. https://doi.org/10.1002/lno.10636.
Tang, S., Chen, C., Zhan, H., Xu, D., 2007. Remotely-sensed estimation of the euphotic depth in the northern South China Sea. Int. Geosci. Remote Sens. Symp. 917–920. https://doi.org/10.1109/IGARSS.2007.4422947.
Turner, J.T., 2015. Zooplankton fecal pellets, marine snow, phytodetritus and the ocean's biological pump. Prog. Oceanogr. 130, 205–248. https://doi.org/10.1016/j.pocean.2014.08.005.